Nano Energy 41 (2017) 476–487

Contents lists available at ScienceDirect

Nano Energy

journal homepage: www.elsevier.com/locate/nanoen

Full paper

Guanidinium thiocyanate selective Ostwald ripening induced large grain for high performance perovskite solar cells

Ngoc Duy Pham[a], Vincent Tiing Tiong[a], Disheng Yao[a], Wayde Martens[a], Antonio Guerrero[b], Juan Bisquert[b], Hongxia Wang[a,*]

[a] School of Chemistry, Physics and Mechanical Engineering, Science and Engineering Faculty, Queensland University of Technology, Brisbane, Australia
[b] Institute of Advanced Materials (INAM), Universitat of Jaume I, 12006 Castelló, Spain

ARTICLE INFO

Keywords:
Perovskite solar cells
Large grains
Improved fill factor
High efficiency
Ostwald ripening

ABSTRACT

Organic-inorganic lead halide perovskite has become one of the most attractive materials for future low-cost high-efficiency solar technology. However, the polycrystalline nature of perovskite thin-film often possesses an exceptional density of defects, especially at grain boundaries (GBs) and film surface, limiting further improvement in the power conversion efficiency (PCE) of the perovskite device. Here, we report a simple method to reduce GBs and to passivate the surface of a methylammonium lead tri-iodide ($MAPbI_3$) film by guanidinium thiocyanate (GUTS)-assisted Ostwald ripening post treatment. High-optoelectronic quality $MAPbI_3$ film consisting of micron-sized grains were synthesized by post-treating a $MAPbI_3$ film with GUTS/isopropanol solution (4 mg/mL, GUTS-4). Analysis of the electrochemical impedance spectra (EIS) of the solar cells showed that interfacial charge recombination resistance of the device based on a GUTS-4 post-treated $MAPbI_3$ absorber film was increased by a factor of 1.15–2.6, depending on light illumination intensity, compared to the control $MAPbI_3$ cell. This is consistent with results of the open-circuit voltage (V_{oc}) decay and the light intensity dependent photovoltage evolution which shows device with GUTS treatment had one order longer charge carrier lifetime and was more ideal (ideality factor = 1.25). Further characterization by Kelvin probe force microscope indicated that GUTS-4 treatment shifted the energetics of the $MAPbI_3$ film by ~ 100 *meV* towards better energy level alignment with adjacent SnO_2 electron transport layer, leading to a more favorable charge extraction process at the $MAPbI_3/SnO_2$ interface. As a result, the PCE of PSCs was enhanced from 14.59% to 16.37% and the hysteresis effect was mitigated.

1. Introduction

Recently, organic-inorganic lead halide perovskites have emerged as ideal materials for low-cost solution-processable, high-efficiency solar technologies [1]. Solar cells based on perovskites have shown skyrocketing progress in power conversion efficiency (PCE) within seven years of development, from 3.8% in 2009 to over 22% in early 2016, making it the most commercially attractive solar cell technology at present [2,3]. The nature of am-bipolar charge transport of perovskite (perovskite materials can transport both electron and hole between cell terminals) [4–6] has led to the development of planar perovskite solar cell configurations in which perovskite functions as both the light absorber and charge transport layers. The structural simplicity of the planar configuration makes it even more economically viable and commercially attractive.

It is recognized that a delicate control of the optoelectronic quality of perovskite film is of vital importance to obtain a high-efficiency solar cell, especially for planar structure [6,7]. For example, pin-holes and incomplete surface coverage can result in low light absorption and low-resistance shunting paths while the high density of undesirable defects causes a high-rate of charge recombination and low charge collection efficiency. This in turn entails low photovoltaic performance of the corresponding devices. To solve this issue, methods for preparing pin-hole-free, uniform and highly compact films have been developed such as the anti-solvent one-step dripping method [7–10]. Fundamentally, the anti-solvent method involves in pouring of an anti-solvent onto a wet perovskite film to induce fast crystallization, resulting in formation of a smooth, fine-grained polycrystalline film which contains significant number of grain boundaries (GBs). Recent reports have suggested that, GBs in perovskite film are likely to function as: 1) centralized areas of electronic trap states and 2) pathways for ion migration [11–13]. The electronic trap states not only serve as barriers for charge transport, but

* Corresponding author.
E-mail address: hx.wang@qut.edu.au (H. Wang).

http://dx.doi.org/10.1016/j.nanoen.2017.10.006
Received 18 August 2017; Received in revised form 15 September 2017; Accepted 2 October 2017
Available online 03 October 2017

they also enhance non-radiative recombination, severely reducing the charge carrier life time, and thus the overall photovoltaic device performance [14–16]. Possibly, the high density of GBs or electronic defects in the perovskite films prepared by typical deposition techniques, including the antisolvent-dripping method, is one of the reasons why the best performing PSCs still lags behind the theoretical Schocley-Queisser efficiency limit for a single junction solar cell [17]. In addition, ion migration at GBs is suspected to cause current-voltage hysteresis of perovskite devices [18]. As such, it is essential to reduce the number of GBs through increasing grain sizes and/or passivating the GBs of perovskite films to enable hysteresis-free high efficiency PSCs.

A variety of methods have been established to eliminate the GBs of perovskite films through the careful control of nucleation-growth rates by modification of underlying substrates [11,19] or altering the chemistry of precursor solutions [20,21]. Among them, methods based on tuning perovskite precursor composition seem to be the most successful. Yang et al. reported that methyammonium iodide (MAI) is an effective additive to tune the grain size of methyammonium lead tri-iodide ($MAPbI_3$) films from few hundred nanometer to few micrometer [20]. Pursuing a different direction, Carmona *et al.* stated that a moderate excess of PbI_2 in the $MAPbI_3$ precursor is beneficial for obtaining large homogeneous $MAPbI_3$ films [22]. Crystal growth retardants, such as lead(II) chloride ($PbCl_2$) have also been shown to be an advantageous precursor additive for grain size enlargement of $MAPbI_3$ films [23,24]. Besides lead(II) halide based additives, non-halide lead source such as lead(II) thiocyanate ($Pb(SCN)_2$) were also reported to be effective for enhancing crystal domain sizes of perovskite films [25–29].

Nevertheless, it is difficult to prepare high optoelectronic quality perovskite film with minimal defect densities, even with anti-solvent dripping method, and thus film post treatment is normally necessary [30–34]. Among these, the method based on post treatment of $MAPbI_3$ perovskite film using methylammonium bromide (MABr)/isopropanol was reported to lead to secondary crystallization of $MAPbI_3$ films through an Ostwald ripening mechanism [32]. The resulting $MAPbI_3$ films have enhanced grain size, crystallinity and yielded better PCE devices. The elegance of this finding is that post-treated perovskite films are pinhole-free, possessing large grain domain and low density of defects regardless of the quality of initial film. However, the $MAPbI_3$ films prepared by the MABr-assisted Ostwald ripening process often contain broad crystal size distributions even though the film has undergone an extreme heat treatment process (i.e. 150 °C for 10 min). To date, only a few Ostwald ripening-assisted precursors have been utilized for the post-treatment of perovskite films due to strict requirements for efficient coarsening in Ostwald-type ripening process [32]. Due to this, there still remains considerable room to explore the application of Ostwald ripening-assisted for improving the quality of perovskite film for higher power conversion efficiency.

Apart from grain size enlargement, approaches for passivation of GBs and interfaces/surface of perovskite film have also been investigated. Fullerene, an electron transport layer, was found to be an effective passivating agent which diffuses along GBs to passivate the defects [35–37]. Several groups have noted that PbI_2 is able to passivate GBs and interfaces of perovskite films [21,38,39]. These studies have shown that PbI_2 mainly occupies the space along GBs of perovskite film, forming an energy barrier that hinders leakage of both electrons and holes from perovskite film which reduces recombination. Furthermore, guanidinium iodide (GuI) was also found to successfully suppressing defects at GBs of $MAPbI_3$ films (more reference) [40]. The use of (GuI) in $MAPbI_3$ precursor solutions has proven to extend the charge carrier lifetime by a factor of ten, and thus yielding PCE exceeding 17% for planar $MAPbI_3$ solar cell. The research showed that guanidinium ions do not incorporate in perovskite lattice, but instead, reside at the GBs of perovskite film, forming hydrogen bonds with under-coordinated iodine species and thus suppressing charge recombination. Although the benefits of GuI for defect mitigation in $MAPbI_3$ films is exceptional, the final structure of Gu-based products remain unclear.

Herein, we report a new method based on treatment of $MAPbI_3$ film using a guanidinium thiocyanate (GUTS) precursor solution. In this study, it was found that the GUTS-treatment effectively converts fined-grain nanometer-scale $MAPbI_3$ film into micron-sized $MAPbI_3$ perovskite film with a low density of GBs. We have also found that this GUTS-post treatment method successfully passivates the perovskite interface, which in turn significantly reduces surface charge recombination. The cooperation of these two effects enables improved performance of solar cells with less hysteresis.

2. Experimental section

2.1. Materials preparation

All materials were purchased from Sigma-Aldrich and used as received without further purification unless otherwise stated. Methylammonium lead tri-iodide ($MAPbI_3$) perovskite films were prepared based on Lewis acid-base adduct approach, details of which are described in the previous reports [9,10]. In brief, a $MAPbI_3$ perovskite precursor solution was prepared by dissolving 461 mg of PbI_2, 159 mg of methylammonium iodide (MAI) (Dyesol), and 78 mg of dimethyl sulfoxide (DMSO) in 650 mg of dimethyl formamide (DMF) at room temperature, under rigorous stirring for four hours to obtain clear solution. The prepared $MAPbI_3$ precursor solution was filtered by a syringe filter (pore size: 0.22 μm) prior to use for deposition of films. Guanidinium thiocyanate (GUTS) precursors were prepared by dissolving different amounts of GUTS (2 mg, 4 mg, 6 mg, 8 mg, and 10 mg) in 1 mL anhydrous isopropanol (IPA). A solution for hole transport material was prepared by addition of 72.3 mg of 2,2′,7,7′-Tetrakis-(N,N-di-4-methoxyphenylamino)-9,9′-spirobifluorene (Spiro-MeOTAD) (Borun New Material), 28.8 μL of 4-*tert*-butylpyridine, and 17.5 μL of Bis(trifluoromethane)sulfonimide lithium (Li-TFSI) solution (720 mg of Li-TFSI in acetonitrile) to 1 mL of chlorobenzene.

2.2. Device fabrication

Solar cells were fabricated using fluorine-doped tin oxide (FTO) coated glass (Nippon Electric Glass, 15 Ω/sq) as substrate which was firstly patterned through partially removal of FTO via etching with 35.5 wt% HCl and zinc powder. The substrates were then cleaned for 20 mins in an ultrasonic bath with an aqueous solution of Decon-90 detergent (5%), followed by the same treatment in a mixture of acetone, isopropanol and ethanol (1:1:1, volume ratio). Prior to use, the substrates were treated with UV-Ozone for 30 mins to remove any remaining organic solvent residue. An electron transport layer based on SnO_2 (~ 40 nm) was deposited via spin-coating 0.1 M solution of tin(II) chloride (98%) in ethanol (96%) at 3000 rpm for 30 s in air by following the procedure reported previously [41]. The film was then annealed in air at 185 °C for 1 h before being cleaned with UV-Ozone for 20 mins and transferred to an Ar-filled glove box. A $MAPbI_3$ layer (~ 400 nm) was deposited onto the prepared SnO_2 layer at 4000 rpm for 25 s. During spin-coating, 0.5 mL of diethyl ether was dropped onto the center of the spinning substrate 18 s prior to the end of the program. The perovskite layer was then dried at 65 °C for 2 mins. For samples treated via the GUTS methodology, 100 μL of GUTS in IPA solution (2–10 mg/mL) was dropped on top of the perovskite film during a second spin coating cycle using one-step program at 4000 rpm for 30 s. The perovskite layer was then annealed at 100 °C for 2 mins. For convenience, the $MAPbI_3$ films with treatments of 2 mg/mL, 4 mg/mL, 6 mg/mL, 8 mg/mL and 10 mg/mL GUTS in IPA are abbreviated as GUTS-x-$MAPbI_3$, where x = 2, 4, 6, 8 and 10. The hole-transport layer (~200 nm) was deposited from the prepared Spiro-OMeTAD solution onto the as-prepared perovskite layer at 4000 rpm for 30 s. The device fabrication was finished by deposition of a 100 nm layer of gold for use as a back contact on the prepared sample via an e-beam evaporation process operating at 10^{-6} Torr pressure.

2.3. Characterization

The top-view and cross-sectional scanning electron microscopy (SEM) images of the samples were obtained using a field emission scanning electron microscope (FSEM JOEL 7001 F) at an acceleration voltage of 5 kV. The UV–visible absorbance spectrum was measured with a UV–visible spectrometer (Cary 50). Crystal structure of the perovskite film deposited on FTO-glass substrate was determined by X-ray diffraction (Rigaku SmartLab) with a monochromatic CuK $\alpha(\lambda = 0.154$ nm) as a radiation source. A scan rate of 1.5°/min and step size of 0.02° was used in the XRD measurement. The performance of perovskite devices was measured under irradiation of 100 mW/cm^2 (AM1.5, 1 sun) provided by a solar simulator (Oriel Sol3A, Newport) equipped with 450 W Xenon lamp. IPCE measurement was conducted by quantum efficiency system (IQE 200B, Newport) under AC mode. Electrochemical impedance spectroscopy (EIS) of the PSCs was performed in a frequency range from 1 MHz to 100 mHz using an electrical workstation (VSP BioLogic Science Instruments) under open-circuit condition with different light illumination intensities. An AC voltage with a perturbation amplitude of 20 mV was applied on the device in the (EIS) measurement. Scanning Kelvin Probe Force Microscopy (KPFM) (Oxford instrument, Asylum Research) was performed on the prepared perovskite film in ambient conditions using NSG-03 Pt coated cantilever at room temperature. Work function of the cantilever was measured using HOPG standard sample.

The open-circuit voltage decay measurements were performed by monitoring the open-circuit voltage (V_{oc}) of PSC as a function of time in dark with an electrochemical workstation (BioLogic). The V_{oc} of the cell was generated using a white light LED with illumination intensity equivalent to 0.15 sun (illumination time: ~ 2 s). The open-circuit

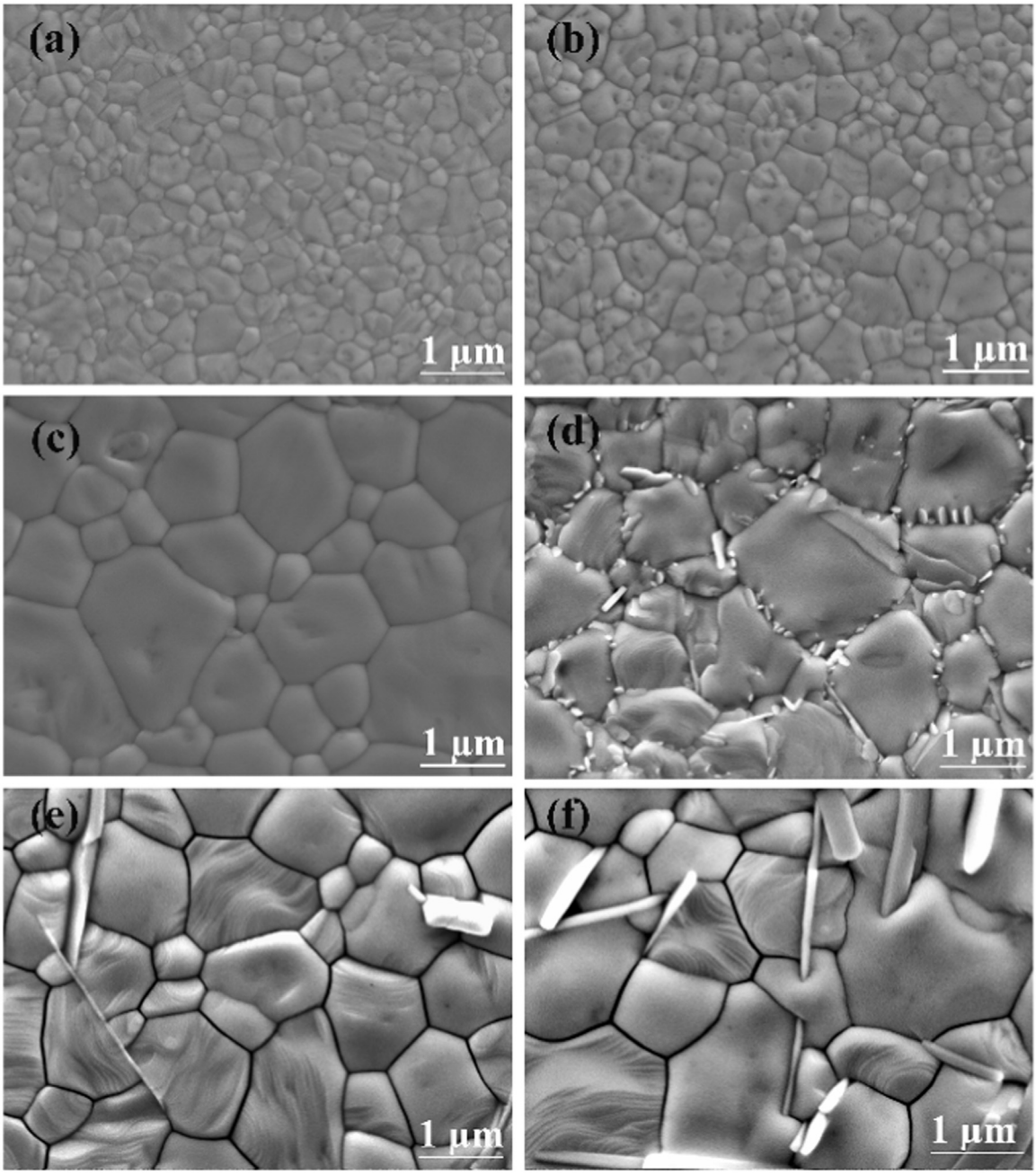

Fig. 1. Top-view SEM images of $MAPbI_3$ films. **(a)** Control $MAPbI_3$ film and the film treated with different concentrations of GUTS/IPA solution **(b)** 2 mg/mL, **(c)** 4 mg/mL, **(d)** 6 mg/mL, **(e)** 8 mg/mL, **(f)** 10 mg/mL.

voltage decay (OCVD) was recorded when the white LED was turned off.

The light intensity dependence of open-circuit voltage (V_{oc}) measurement was carried out by measuring *J-V* plots of the solar cell under different illumination intensities generated by the solar simulator. The light intensities were controlled by using neutral density optical filters with transmittance of 1%, 11%, 19%, 30% and 55%.

The stability of the PSCs was tested by monitoring the efficiency of un-encapsulated PSCs which were stored in a desiccator (relative humidity ~ 33–35%) in dark. The performance of the device was measured every 3 days in ambient condition with relative humidity of 40–60%.

3. Results and discussion

Fig. 1(a)-(f) illustrates the top-view scanning electron microscopy (SEM) images of GUTS-x-$MAPbI_3$ perovskite films with x = 0, 2, 4, 6, 8, 10, respectively. In accordance to the previous reports [9,10], $MAPbI_3$ film synthesized by our one-step Lewis acid-base adduct method is pinhole-free, highly compact with crystallite sizes ranging from 100 nm to 500 nm (Fig. 1a). When $MAPbI_3$ films were treated with GUTS-2 precursor (2 mg/mL GUTS in isopropanol (IPA)), larger grains with domain size up to 800 nm were observed while the $MAPbI_3$ film remains uniform and compact (Fig. 1b). Upon increasing the concentration of GUTS to 4 mg/mL (Fig. 1c), clear evidence of grain growth is seen with most grains exceeding 1 μm. Compared to the pristine $MAPbI_3$ film, the lateral crystallite size of GUTS-4-$MAPbI_3$ film is five-folds larger, suggesting the effectiveness of this simple post processing procedure. As a general indication, the larger the perovskite film crystals, the higher the solar cell performance is expected because perovskite films with larger grains have lower numbers of GBs which act as barriers for charge transport between the cathode and anode in PCS [11,12,28]. With further increment of the GUTS concentration to 6 mg/mL, 8 mg/mL and 10 mg/mL, even larger grain sizes are observed (~ 2 μm in average with GUTS-10 treated film). However, pronounced contrast along GBs and surface of $MAPbI_3$ film are observed, which suggests formation of secondary phases. The amount of secondary phases increased as the concentration of GUTS increased, which is more clearly shown at lower magnification SEM images (Fig. S1). We conducted SEM-EDS mapping to determine the elementary composition over the area of grain interior and grain boundaries. The results show the atomic ratio of I/Pb is very similar (2.87–2.89) at both areas (Fig. S2, Table. S1), suggesting the bright small crystals in the grain boundaries are probably intermediate phase with atomic ratio of I/Pb similar to the perovskite material. Furthermore surficial wrinkles are also found on the $MAPbI_3$ grains as the concentration of GUTS exceeded 6 mg/mL (Fig. 1d-f). The appearance of these wrinkled textures is likely induced by strain due to massive $MAPbI_3$ grain coarsening and/or competitive grain growth of $MAPbI_3$ crystals and secondary phases [10], which may lead to high surface roughness.

Before further characterization of optoelectronic properties of the $MAPbI_3$ film, we first investigated the fundamental reason for the significant morphological change in the films. With the knowledge that IPA is capable of dissolving $MAPbI_3$ via MAI-extracting (1) [42,43], we presume that this extraction is the initial stages of Ostwald ripening which could be the potential origin for the above morphological change.

$$CH_3NH_3PbI_3\ (IPA) \leftrightarrow CH_3NH_3I + PbI_2 \quad (1)$$

According to the Ostwald ripening process, once the GUTS/IPA solution is introduced to the surface of $MAPbI_3$ film, unstable small $MAPbI_3$ crystals with high surface energy will be partially dissolved into the IPA, giving up their mass so that large stable crystals can grow [32,44]. In this mechanism, the dissolution/de-nucleation rate of the unstable small $MAPbI_3$ crystals (depending on solubility capacity of solvent used) is extremely crucial because it determines the growth rate coefficient of stable large $MAPbI_3$ crystals [45]. In other words, the higher rate of de-nucleation/dissolution, the higher is the rate of crystal growth, and thus larger crystal size could be obtained according to the following equation:

$$Z(D_N, G) = 1.1(D_N \times G)^{-0.5} \quad (2)$$

where $Z(D_N, G)$ is the number of crystals per unit area, which is inversely proportional to the crystal size, D_N is de-nucleation rate of unstable small crystals and G is growth rate of stable large crystals.

To verify our hypothesis, we examined the effect of IPA-only post treatment on the morphology of $MAPbI_3$ film. We found that marginal grain size enhancement was observed with the $MAPbI_3$ film treated with IPA (Fig. S3) which is consistent with a recent study [32]. We infer that the extremely low solubility of $MAPbI_3$ in IPA leads to a low rate of de-nucleation/dissolution of unstable small $MAPbI_3$ crystals, and thus inefficient coarsening process. It has been reported by Yang et al. that methylammonium bromine (MABr) is able to tackle the problem as it favours the dissolution reaction (1) [32]. However, as stated, the intercalation of MABr and/or the I/Br exchange reaction could competitively take place, inhibiting the dissolution reaction, which in turn restricts effective Oswald ripening of $MAPbI_3$ film.

Similar to Br^- anion, SCN^- anion has stronger interaction with Pb^{2+} cation compared with I^- anion, thus one can expect that GU-SCN/IPA may follow the same grain coarsening mechanism as does by MABr/IPA [46]. However, as shown in Fig. S4, compared to MABr/IPA treatment, a $MAPbI_3$ film prepared by GUTS/IPA treatment is smoother with grain sizes two-folds larger on average and a narrower grain size distribution. In addition, micron-sized $MAPbI_3$ grains were easily formed by using the GUTS post treatment even without heat treatment (Fig. S5), indicating that the Ostwald ripening process enabled by the GUTS/IPA treatment is very effective. More interestingly, there is no concentration window for GUTS/IPA which is required to control the size of $MAPbI_3$ grains. Instead, the higher of the concentration of GUTS/IPA is used, the larger grain is observed (Fig. 1 and Fig. S6). The above observations lead us to conclude that besides the dissolution-assisted effect of GUTS (as similar to MABr), there must be another source that aids the grain growth. There is a possibility that there is a reaction of GUTS/IPA and $MAPbI_3$ as follows:

$$CH_3NH_3PbI_3 + GU{-}SCN \rightarrow (GuI(s){+}PbI_2(s)) + (CH_3NH_2(g) + HSCN(g)\uparrow) \quad (3)$$

The unstable HSCN (gas) is probably expelled from the film rapidly [28] since we could not detect any observable signal of sulfur by X-ray photoelectron microscopy (XPS), inductively coupled plasma spectroscopy (ICP-MS) and Fourier transform infrared spectroscopy (FTIR) (not shown here). The produced PbI_2 and GuI and/or a compound formed by them ($(GuI)_x(PbI_2)_y$) accumulates at the surface and GBs of $MAPbI_3$ film as the secondary phases according to Fig. 1e-f. It is very likely that the as-formed CH_3NH_2 (MA) gas can dissolve $MAPbI_3$ crystal more efficiently than IPA, as suggested by previous reports [33,47–50]. We therefore propose that the formed MA (gas) enhances the rate of de-nucleation and increases the solubility of unstable small $MAPbI_3$ crystals which in turn facilitates the grain coarsening. Compared to conventional method of Ostwald ripening, the dissolution of small-sized $MAPbI_3$ crystals enabled by GUTS/IPA post treatment in this work is extremely fast and effective. As a result, the process is easier and more efficient to form large grain in the $MAPbI_3$ film. A comparison is outlined in Fig. 2.

We have further found that incorporating GUTS into $MAPbI_3$ precursor solution does slightly enlarge domain size of $MAPbI_3$ films as illustrated in Fig. S7a-d. However, compared to GUTS post-treated $MAPbI_3$ film, those with GUTS additive in perovskite precursor are two-folds smaller in terms of domain size (Fig. S7d versus Fig. 1c). Besides, adding GUTS additives to the $MAPbI_3$ precursor leads to the formation

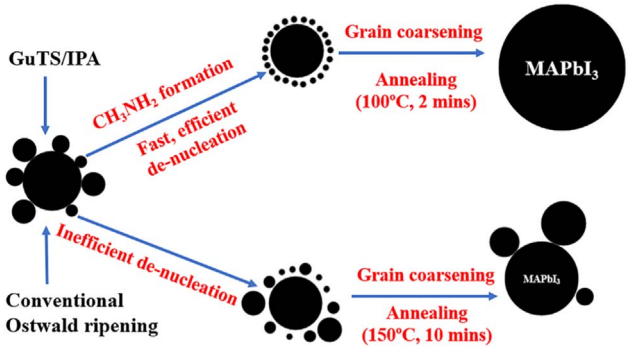

Fig. 2. Schematic illustration of Ostwald ripening process for the $MAPbI_3$ perovskite crystal growth assisted by GUTS in this work and by conventional method.

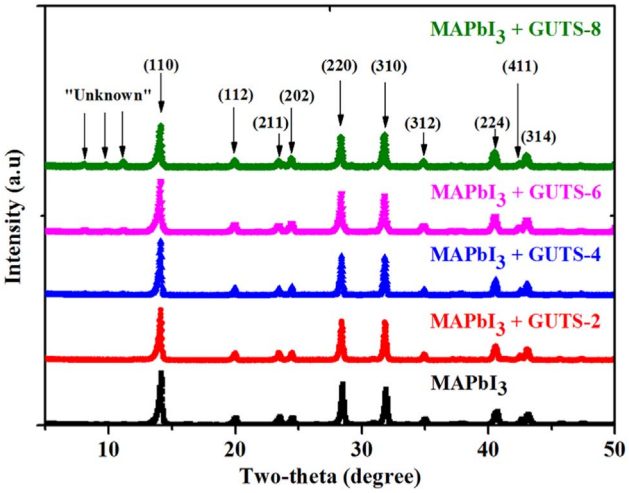

Fig. 3. XRD patterns of $MAPbI_3$ films with and without GUTS treatment.

of a considerable impurities on surface of $MAPbI_3$ film as shown in Fig. S7(b, c, d), reducing the optoelectronic quality of the films. We therefore propose that GUTS-assisted Ostwald ripening post-treatment could be the best procedure for fabricating $MAPbI_3$ film with the optimal morphology.

In order to identify the effect of SCN^- anions and guanidinium cations on the morphology of $MAPbI_3$, we prepared $MAPbI_3$ film from a precursor which contained 5% $Pb(SCN)_2$ (molar ratio) in relative to PbI_2. We have found that the film with 5% $Pb(SCN)_2$ in the $MAPbI_3$ precursor consisted of ~ 4 times larger grain sizes compared to the control $MAPbI_3$ film, confirming the effectiveness of SCN^- anion in terms of grain size enlargement. However, a large amount of secondary phases accumulated near grain boundary region of the film can be clearly seen (see Fig. S8b). This is in accordance with the recent report in literature [28]. In a parallel experiment, we studied the effect of guanidinium cations on the grain evolution of $MAPbI_3$ by using different amount of guanidinium iodide (4 mg/mL and 6 mg/mL) in isopropanol solution in the post treatment of $MAPbI_3$ film. We have found that the grain sizes of GuI-treated $MAPbI_3$ film are slightly larger than the control $MAPbI_3$ film (Fig. S8a, c, d). Furthermore, the film retained the uniformity and compactness of the original $MAPbI_3$ film. The above results indicate that both SCN^- anion and guanidinium cation play important roles in the grain size evolution of $MAPbI_3$ film.

The absorption spectra of $MAPbI_3$ films prepared from different GUTS concentrations (Fig. S9) show characteristic absorption onset at around 770 nm regardless of GUTS concentration, indicating that the band gap of $MAPbI_3$ is not affected by GUTS treatment. Below 4 mg/mL GUTS in IPA, the $MAPbI_3$ film has slightly higher light absorption coefficient than the pristine one, suggesting an improved film crystallinity. Beyond that, the absorbance of $MAPbI_3$ films is reduced which can be ascribed to the formation of a substantial amount of secondary phases (as shown in Fig. 1d-f).

X-ray diffraction (XRD) was used to structurally characterize the material phases in the $MAPbI_3$ films with and without GUTS-treatment (Fig. 3). As indexed in Fig. 3, the main peaks of all the films can be well assigned to the reflection of $MAPbI_3$. It should be noted that the peak intensity ratio between (220) and (310) plane changes as concentration of GUTS increases, indicating the change in growth rate of the two crystallographic plane of $MAPbI_3$ crystals. This change could also be associated with the formation of secondary phases, which might alter crystal growth rate at particular direction. In addition, weak diffraction peaks at 8.12°, 9.82°, and 11.2° are observed when the concentration of GUTS for post treatment is over 6 mg/mL, which should be assigned to the observed secondary phases observed in top-view SEM images (Fig. 1d-f).

To identify these unknown peaks, we collected XRD patterns of GuSCN (powder), GuI (powder) and "$GuPbI_3$" films (Fig. S11) because they are most likely the by-products of the reaction (3). A yellow $GuPbI_3$ film was prepared by spin-coating a precursor of GuI:PbI_2:DMSO (1:1:1, molar ratio) in DMF followed by annealing at 100 °C for 2 mins. It is worth highlighting that no peak from GU-SCN was found in the diffraction patterns of GUTS-treated $MAPbI_3$, indicating that GU-SCN was completely consumed in the reaction (3) with $MAPbI_3$. In addition, the unknown peaks do not match any diffraction patterns of GuI or "$GuPbI_3$" phases either, suggesting that the by-products induced by reaction (3) (probably GuI and PbI_2) combined with each other to form intermediate phases $(GuI)_x(PbI_2)_y$, located at the GBs or/and the surface of $MAPbI_3$ film, in accordance with previous observation [40]. According to Ref [40], a tiny amount of the intermediate phases are not harmful to the resulting device performance, instead they could passivate the GBs/surface defects. We therefore have not intentionally excluded the subtle amount of the intermediate phases in the $MAPbI_3$.

Having shown that micron-sized $MAPbI_3$ films could be easily obtained through manipulation of the concentration of GUTS in the post treatment process, we proceed to integrate these films into solar cells. The performance of these $MAPbI_3$ devices is compared and listed in Table 1.

When the $MAPbI_3$ absorber layer was post treated with GUTS/IPA with concentration up to 4 mg/mL, the average power conversion efficiency (PCE) of the solar cells increases by nearly 20%, from 12.7 ± 1.8% to 15.2 ± 0.9%, mainly due to the increase of open-circuit voltage (V_{oc}), from average 1.02 ± 0.03 V to average 1.06 ± 0.0.02 V, and fill-factor (*FF*), from 60 ± 5% to 68 ± 3% (Table 1). These results are consistent with the observed reduction of the series resistance (R_s) by ~ 37%, and the significant increase of shunt resistance (R_{sh}) by six-folds of the devices (Table 1). The lower R_s implies the perovskite film has lower inter-particle contact resistance, higher internal film conductivity and better contacts with selective charge transport layers, while the larger R_{sh} indicates the greater surface and GBs passivation [10,51]. In addition, slightly higher current densities are also witnessed as the GUTS precursor concentration increases, which is consistent with the UV–visible light absorption spectrum (Fig. S9 and Fig. S10). However, further increase of the GUTS content up to 8 mg/mL leads to a dramatic reduction of all photovoltaic parameters even though grain size of the $MAPbI_3$ film was increased (Table 1). This is probably related to the formation of large quantities of secondary phases in the film and the increase in the roughness of top surface of the perovskite film as shown in Fig. 1d-e), which are believed to not only reduce the light absorption of $MAPbI_3$ film (Fig. S9), but also cause current leakage, resulting in low solar cell performance. The above SEM, XRD, UV–vis absorbance and PCE data suggest that the best-performing device (GUTS-4-$MAPbI_3$ based solar cell, 15.2 ± 0.8%) is only enabled by a synergetic effect of $MAPbI_3$ film morphology, crystallinity and the amount of incorporated secondary phases. In the next section, we will

Table 1
Characteristic photovoltaic parameters of $MAPbI_3$ solar cells with different concentration of GUTS in the post treatment process.

Cell	PCE (%)	J_{sc} (mA/cm^2)	V_{oc} (V)	*FF* (%)	R_s (Ω/cm^2)	R_{sh} (kΩ/cm^2)
Reference	12.7 ± 1.8	20.7 ± 0.8	1.02 ± 0.03	60 ± 5	53 ± 5	1.5 ± 0.7
GUTS-2	13.5 ± 1.5	20.7 ± 0.5	1.04 ± 0.03	63 ± 4	44.0 ± 3.3	3.4 ± 0.9
GUTS-4	15.2 ± 0.9	21.1 ± 0.3	1.06 ± 0.0.02	68 ± 3	33 ± 2.9	9.1 ± 1.1
GUTS-6	13.9 ± 1.1	20.6 ± 0.38	1.04 ± 0.03	65 ± 2	38.1 ± 3.8	5.2 ± 1.4
GUTS-8	10.9 ± 2	19.5 ± 0.45	0.97 ± 0.05	58 ± 6	62.8 ± 6.6	2.1 ± 1.7

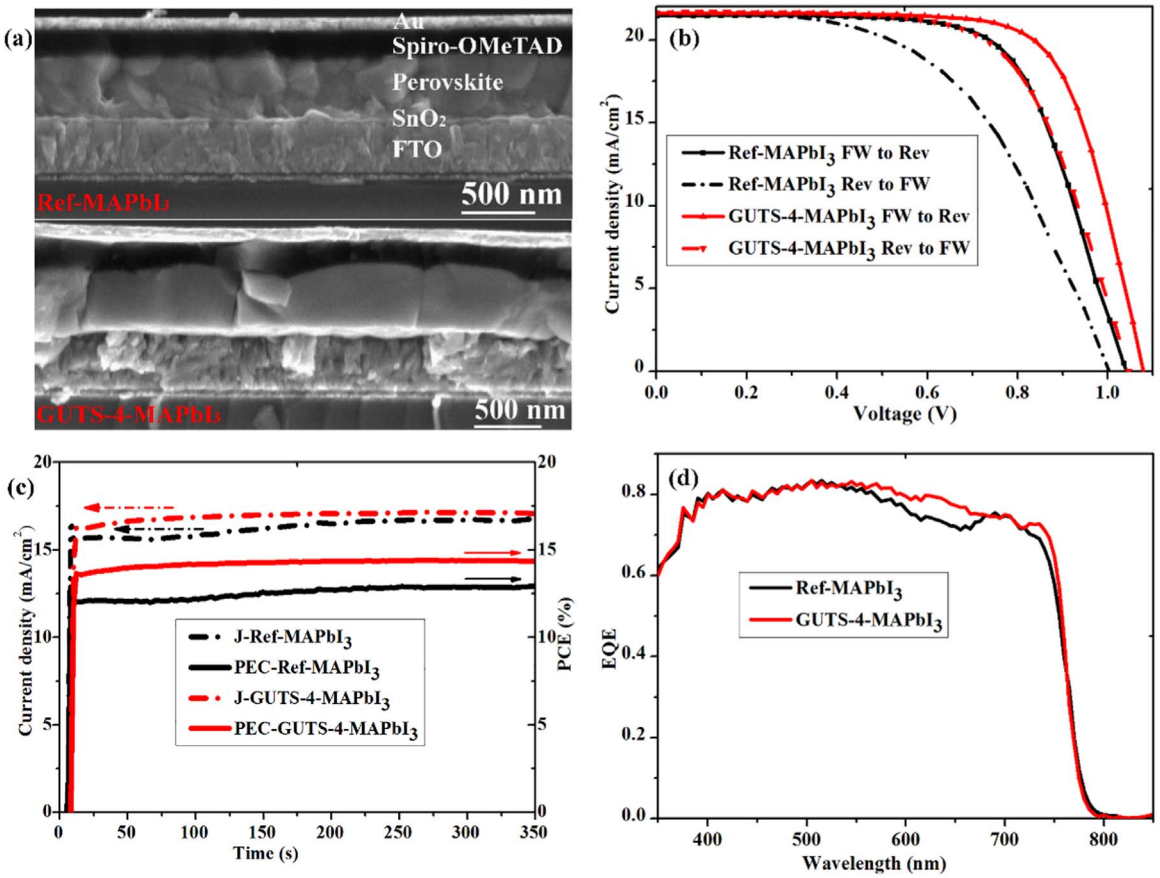

Fig. 4. (a) Cross-sectional SEM images of the completed pristine $MAPbI_3$ and GUTS-4-$MAPbI_3$ solar cells; (b) *J-V* curves of $MAPbI_3$ solar cells with and without GUTS-4 treatment, under reverse and forward voltage scan; (c) stabilized photocurrent measurement at a bias voltage (0.78 V for the pristine $MAPbI_3$ device and 0.85 V for the GUTS-4-$MAPbI_3$ device) at maximum power point and stabilized power output under 1 sun light illumination; and (d) corresponding EQE spectra. (For interpretation of the references to color in this figure legend, the reader is referred to the web version of this article).

provide more insights into the effect of GUTS-4 treatment on the photovoltaic performance and electronic properties of the resultant solar cells.

Fig. 4a shows the detailed cross-sectional SEM of n-i-p planar solar cell with Ref-$MAPbI_3$ (top) and with GUTS-4-$MAPbI_3$ (bottom) absorber layer. In general, both cells consist of a $MAPbI_3$ absorber (~ 400 nm) inserted between a SnO_2 electron transport layer (~ 40 nm) and a Spiro-OMeTAD based hole transport layer (~ 200 nm with current collector of FTO glass and gold. As illustrated, unlike the Ref-$MAPbI_3$ layer which comprises of grains with variable sizes, the GUTS-4-$MAPbI_3$ layer is consisted of a monolithic $MAPbI_3$ layer, attesting the low density of GBs/defects, and thus superior solar cell performance.

The significant reduction of GBs/defects within the $MAPbI_3$ film leads to a 12.2% improvement in the performance of the champion devices (Fig. 4b). In particular, the Ref-$MAPbI_3$ device shows a maximum PCE of 14.59% (11.5%), with a V_{oc} of 1.041 V (1.0 V), a J_{sc} of 21.46 mA/cm^2 (21.5 mA/cm^2) and *FF* of 65% (53%) under reverse (forward) scan respectively. In contrast, the GUTS-4-$MAPbI_3$ solar cell produced a PCE 16.37% (14.21%), with a V_{oc} of 1.077 V (1.043 V), a J_{sc} of 21.6 mA/cm^2 (21.63 mA/cm^2) and *FF* of 70.4% (65%) under a similar measurement protocol. The performance enhancement extracted from the *J-V* curves is also in line with the stabilized PCE shown in Fig. 4c, where the stabilized PCE of the $MAPbI_3$ cell is raised by 11.6% (from ~ 12.9% to ~ 14.5%) with GUTS-4 post treatment. More interestingly, along with device performance enhancement, the degree of current voltage hysteresis defined as $H = 100\% \times (PCE_{rev} - PCE_{fw})/PCE_{rev}$ (where PCE_{rev} and PCE_{fw} are the power conversion efficiency of the device in reverse and forward scan respectively) is also suppressed with value decreases from 21% of Ref-$MAPbI_3$ solar cell to only 13% of GUTS-4-$MAPbI_3$ counter-part.

The Ref-$MAPbI_3$ cell exhibits a high external quantum efficiency (EQE) (over 70%) across a broad wavelength range from 400 nm to 750 nm, with the maximum EQE value of ~ 83% at ~ 500 nm and a depression around 650 nm (Fig. 4d, black curve). The depression in EQE spectrum is common for planar $MAPbI_3$ thin-film solar cell, possibly due to the light-field interference associating with short charge carrier lifetime of the material [52]. Remarkably, this depressed region is greatly filled up when the $MAPbI_3$ absorber was treated with GUTS-4

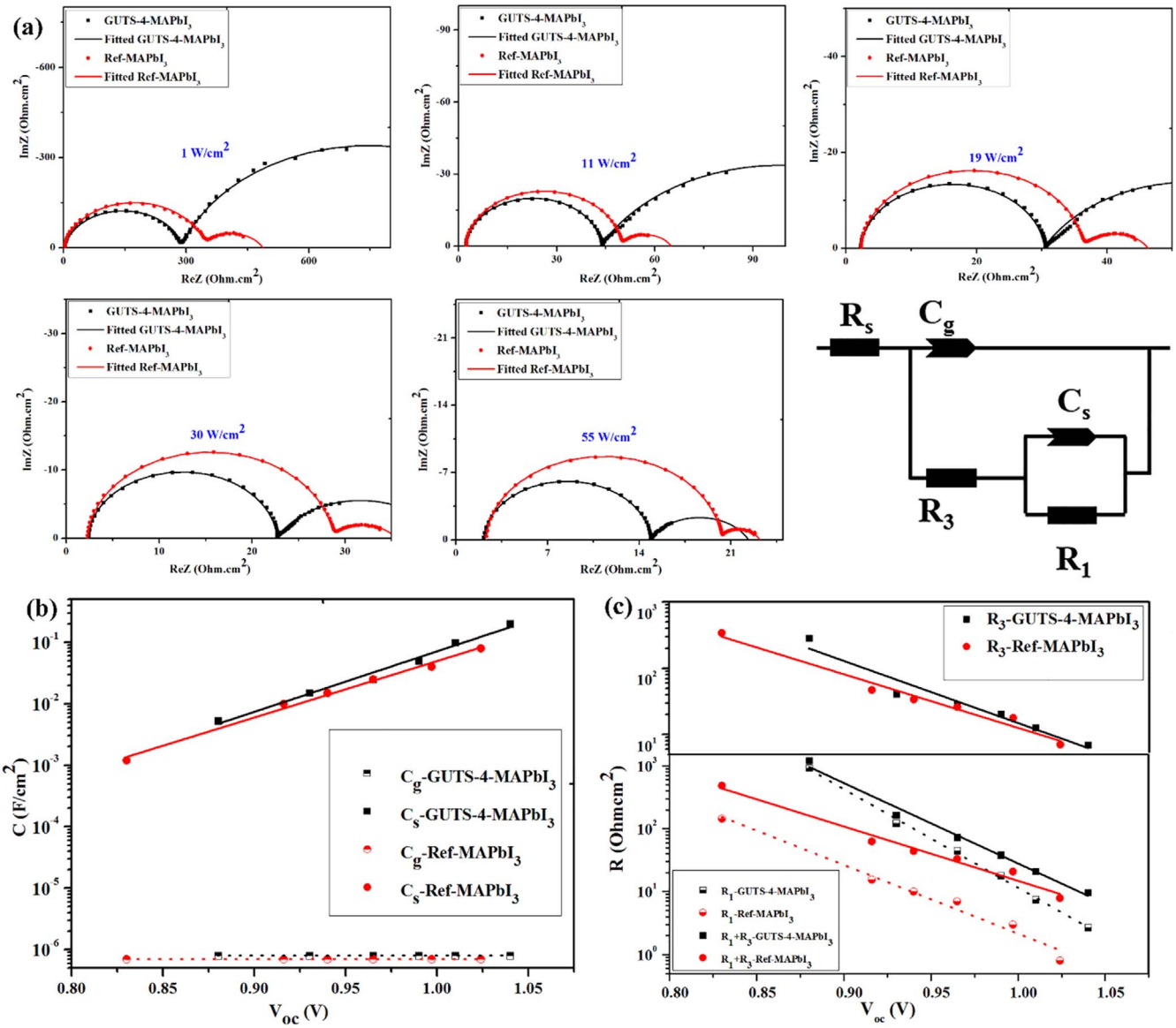

Fig. 5. (**a**) Nyquist plots of Ref-$MAPbI_3$ solar cell (circle red) and fitting (red line), and GUTS-4-$MAPbI_3$ (square black) and fitting (black line) under various light illumination intensities; and equivalent circuit (bottom right). (**b**) Extracted capacitance and (**c**) resistance. (For interpretation of the references to color in this figure legend, the reader is referred to the web version of this article).

as shown in Fig. 4d (red curve), indicating an improvement in charge carrier lifetime. As a result, the integrated current density of GUTS-4-$MAPbI_3$ cell based on the EQE plot is greater than the Ref-$MAPbI_3$ cell (19.3 mA/cm^2 vs 18.8 mA/cm^2, respectively), which is consistent with the J_{sc} obtained in the *J-V* measurement.

Since the main enhancement of device performance are V_{oc} and *FF*, owing to the plunge of the series resistance and the soar of shunt resistance of the device (Table 1), we speculate that the GUTS post treatment probably enhances the electronic properties of the perovskite film towards reducing charge recombination rate. Aiming to interpret the dynamics of charge transfer and recombination in the solar cell devices and to verify this hypothesis, impedance spectroscopy (IS) measurements were conducted at open-circuit condition (~ V_{oc} bias) with various light illumination intensities [53].

The IS spectrum shows two semi-circles in the Nyquist plot. The IS spectrum can be well-fitted using the equivalent circuit shown in Fig. 5a (bottom right). In the equivalent circuit, the capacitive element, C_g, at high-frequency region, represents the dielectric properties of the perovskite absorber layer while the resistive element, R_3, is associated with the transport resistance of electron along the perovskite layer interface. C_s and R_1 obtained at low-frequency region correspond to the properties of perovskite interfaces. More specifically, C_s serves as ionic accumulation capacitance (in dark) or electronic accumulation capacitance (under light illumination) at electrode interfaces, while R_1 coupled with R_3 determines surface recombination resistance [53–55]. The extracted information from the IS fitting for both types of devices shows that the bulk capacitance, C_g, is unchanged regardless of light illumination intensities but the interfacial charge accumulation capacitance, C_s, increases linearly with the illumination intensity (Fig. 5b), while the resistive parameters follow the inverse trend with the illumination intensity (Fig. 5c).

It is found that, compared to the Ref-$MAPbI_3$ solar cell, the interfacial capacitance, C_s, of the GUTS-4-$MAPbI_3$ is slightly higher under light illumination, indicating a slightly higher level of electronic accumulation or higher carrier density at electrode interface. It has been reported that V_{oc} of perovskite solar cell follows the trend with the C_s because under light illumination, the C_s can be proportionally associated with the density of minority carriers at perovskite interface [55]. The IS result observed in the darkness shows that both devices have similar C_s, implying the same level of ionic accumulation at perovskite

interface (Fig. S12 and Table S2, Supplementary). This result also suggests that the higher carrier density at SnO_2/perovskite interface (the perovskite/Spiro-OMeTAD interface can be regarded as ohmic contact) of the GUTS-4-$MAPbI_3$ cell could be due to the longer carrier lifetime. This interpretation of the C_s is in good agreement with the slight increase of open-circuit voltage observed with the GUTS-4-$MAPbI_3$ samples.

Fig. 5c illustrates that the resistance, R_3, of the GUTS-4-$MAPbI_3$ solar cell is slightly larger than that of the reference cell at the same V_{oc} (Fig. 5c, upper). Nevertheless, when we use illumination as the reference, we have found that R_3 of the GUTS-4-$MAPbI_3$ solar cell is slightly smaller than that of the reference cell (Fig. S13). The ratio of R_3 of the $MAPbI_3$ cell to the GUTS-4-$MAPbI_3$ is in the range of 1.01 and 1.29. For example, at 1 mW/cm^2, the ratio is ~ 1.2 while at 11 mW/cm^2, 19 mW/cm^2, 30 mW/cm^2, 55 mW/cm^2 and 100 mW/cm^2 illumination intensities, this value is 1.15, 1.21, 1.29, 1.4 and 1.01, respectively (Fig. S13). The large R_3 of GUTS-4-$MAPbI_3$ device at constant voltage indicate that the GUTS-4-$MAPbI_3$ film has less trap-related recombination and geometrical combination owing to better contact with SnO_2 layer than the pristine $MAPbI_3$ film. Combining this to the fact that the $MAPbI_3$ film with GUTS-4 treatment has much less GBs compared to the reference $MAPbI_3$ film (Fig. 1a, c), we conclude that, the GBs probably serve as barriers for charge transport (in both the bulk and the perovskite interfaces). Once these barriers are eliminated, charge carrier can transport to SnO_2 more efficiently. However, compared to the reference cell, the GUTS-4-$MAPbI_3$ cell has higher low frequency resistance, R_1, (Fig. 5c, bottom). Interestingly, the surface recombination resistance which is the sum of R_1 and R_3, $R_1 + R_3$, of the GUTS-4-$MAPbI_3$ device is larger than the pristine sample, being consistent with the enhanced device performance (Table 1). For instance, compared to the Ref-$MAPbI_3$ device, the surface recombination resistance of the GUTS-4-$MAPbI_3$ counter-part is ~2.5-folds, 2.6-folds, 1.66-folds, 1.15-folds and 1.23-folds larger as light illumination intensity increases from 1 mW/cm^2 to 100 mW/cm^2, respectively (Fig. 5c). The ideality factor of the solar cells extracted from the plots of resistance vs voltage are calculated according to the equation [56].

$$R_{rec}(V) = R_{rec0} e^{\frac{-qV}{m_d k_B T}} \quad (4)$$

Fitting the resistive impedance (Fig. 5b, c) shows that both solar cells have an ideality factor exceeding 1, and the GUTS-4-$MAPbI_3$ cell has lower ideality factor than the pristine device. For example, the fitted R_1, R_3 curves of the ref-$MAPbI_3$ are 1.75, 2.08, respectively, while those of the GUTS-4-$MAPbI_3$ are only 1.65, 1.8, respectively. The value of ideality factor is also indicative of dominance of surface recombination in the both cells [56]. The above IS results indicate that the trap-related recombination which probably occurs at the grain boundaries is significantly suppressed in GUTS-4-$MAPbI_3$ film, and its surface is efficiently passivated compared to the Ref- $MAPbI_3$.

For the analysis of the capacitance we use the expression:

$$C = C_0 e^{qV/m_c k_B T} \quad (5)$$

The fitted C_s, curves of the ref-$MAPbI_3$ show m_c = 1.83, while those of the GUTS-4-$MAPbI_3$ are 1.75. These number close to m_c indicate an accumulation capacitance as suggested by Zarazua et al. [55].

By analysing the open-circuit voltage as a function of light illumination intensity (Fig. 6a), we confirm that besides direct/radiative recombination, trap-assisted recombination exists in both the GUTS-4-$MAPbI_3$. The ideality factor, m_Φ, of both cells were calculated according to Eq. (6) [56].

$$V_{oc} = \frac{m_\Phi k_B T}{q} \ln(\Phi_{ph}) \quad (6)$$

The results $m_{\Phi 1}$ = 1.46 for the reference cell and $m_{\Phi 2}$= 1.25 for GUTS-4-$MAPbI_3$ cell are greater than 1 [57,58]. However, compared to the reference cell, the contribution of trap-assisted recombination is smaller in the GUTS-4-$MAPbI_3$ cell since $m_{\Phi 2} < m_{\Phi 1}$, which is consistent with the value of enhanced shunt resistance and surface charge recombination resistance of the device as shown above. We note that the ideality factors derived from the open-circuit voltage as a function of light illumination intensity results are slightly higher than those extracted from IS results. This slight discrepancy is probably due to the accumulation of ion/electronic carrier at contact under IS measurement [56].

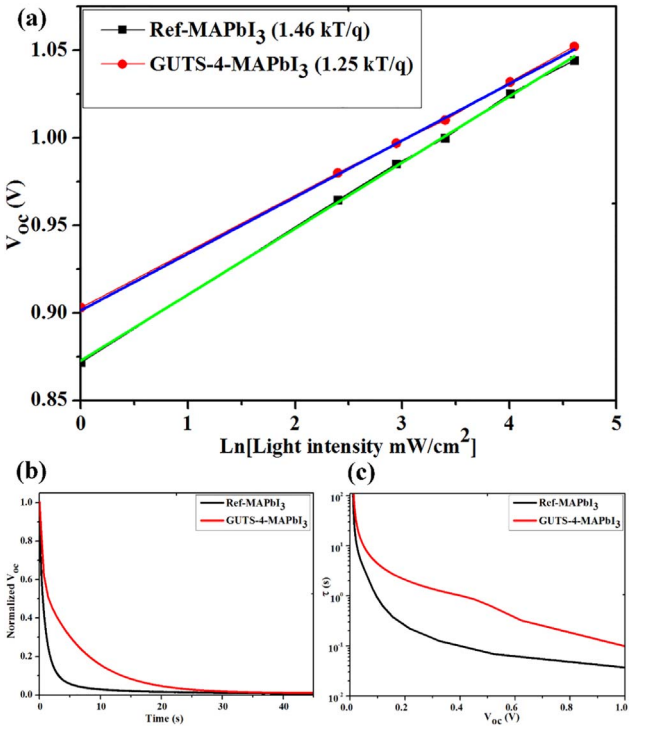

Fig. 6. Open-circuit voltage (V_{oc}) as a function of light illumination intensity (a); V_{oc} decay (b); and instantaneous relaxation time of the reference and GUTS-4-$MAPbI_3$ cells (c). (For interpretation of the references to color in this figure legend, the reader is referred to the web version of this article).

Photovoltage decay is another effective method to investigate the recombination in perovskite solar cells. Fig. 6b illustrates the decay of V_{oc} as a function of time upon removal of light illumination. Basically, a longer decay time of V_{oc} is indicative of longer charge carrier life time [59,60], as can be found by the following equation [59].

$$\tau ir = (-\frac{1}{V}\frac{dV^{-1}}{dt}) \quad (7)$$

where τ_{ir} is instantaneous relaxation time and dV/dt is the decay rate of V_{oc}. The V_{oc} of both types of cells drops to nearly zero within 25 s (Fig. 6). However, the GUTS-4-$MAPbI_3$ cell shows a much slower decay pattern (Fig. 6b, red curve). The instantaneous relaxation time which was calculated from Eq. (7) is plotted in Fig. 6c. It is clearly shown that the instantaneous relaxation time of the GUTS-4-$MAPbI_3$ device is ~one order longer than the pristine sample which is indicative of a prolonged recombination period, in accordance with the larger surface capacitance, C_s observed in IS (Fig. 5b). This result again confirms that the perovskite interface contacts have been improved with GUTS-4 post treatment. We are aware that light soaking prior to V_{oc} decay measurement can give an electrostatic contribution to the photovoltage of PSCs as reported previously [61]. In our case, an illumination pulse with duration of ~ 2 s provided by a white light LED with low intensity equivalent to 0.15 sun was used. Therefore, we can rule out the electrostatic-assisted photovoltage decay effect. As suggested by Gottesman et al. that the interface of perovskite and selective contacts play a key role in the V_{oc} decay pattern [61], we correlate this prolonged duration

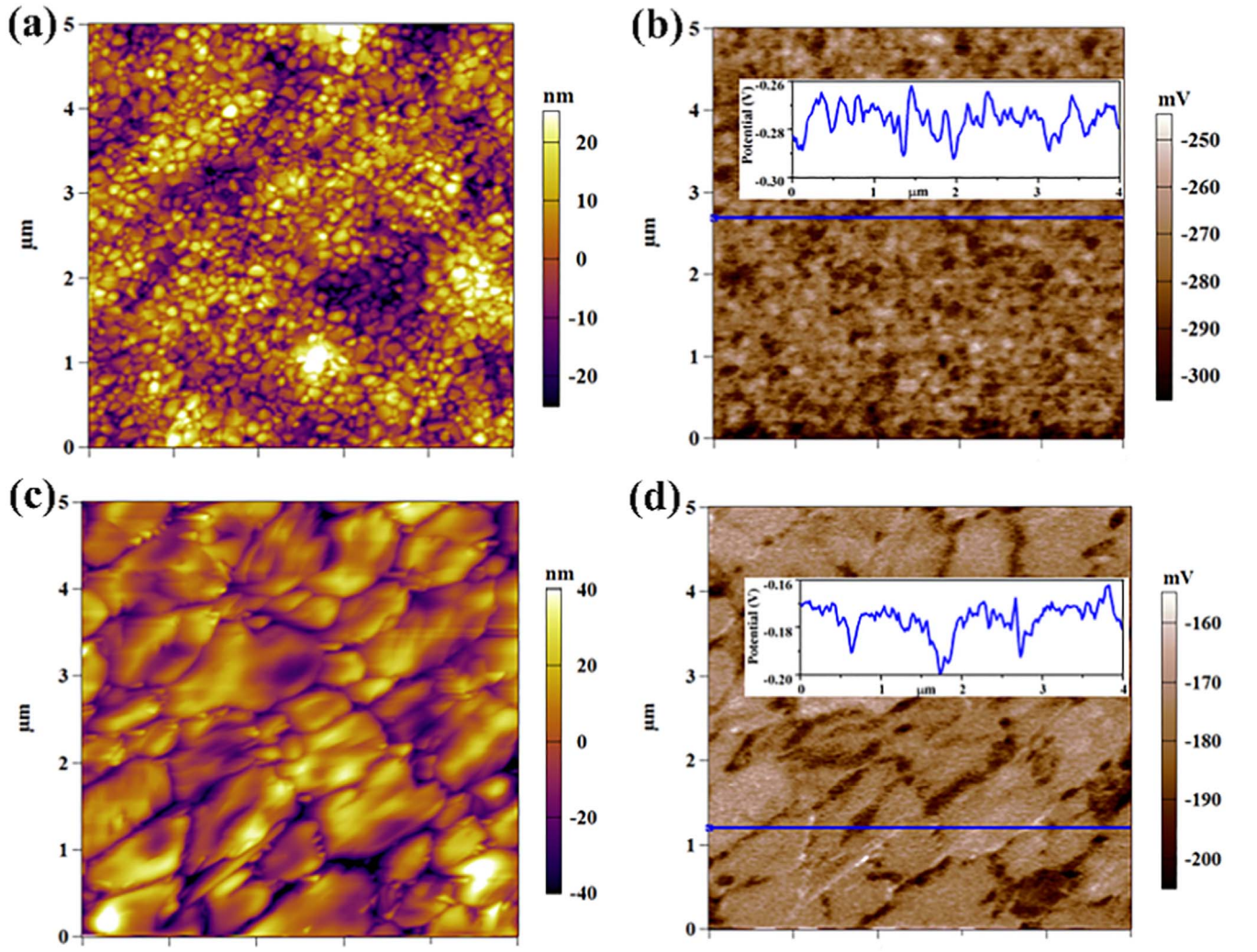

Fig. 7. KPFM topography of (a) Ref-$MAPbI_3$/SnO_2/FTO-glass film and (c) GUTS-4-$MAPbI_3$/SnO_2/FTO-glass film; (b) and (d) are the corresponding contact potential difference (CPD) images.

of voltage decay to the improvement of perovskite interfaces besides the decrease of defect in the bulk of the perovskite layer.

We carried out Kelvin probe force microscopy (KPFM) measurements to study the electronic properties of $MAPbI_3$ surface. KPFM topography of these films showing in Fig. 7a, c is in excellent agreement with the top-view SEM shown in Fig. 1a, c. The micrographs show that although the grain coarsening slightly increases the surface roughness of the $MAPbI_3$ film from 8.87 nm to 12.91 nm, it effectively enlarges the grain size of GUTS-4-$MAPbI_3$ while maintaining film uniformity over a large area ($5 \times 5\ \mu m^2$) (Fig. 7a, c).

The mean value of contact potential differences (CPD) of the GUTS-4-$MAPbI_3$ film is 0.1 V higher than the reference sample, indicating a down-shifted of the electron quasi-Fermi level of the perovskite film (Fig. 7b, d). It has been reported that the conduction band of SnO_2 layer is ~ 170 meV below that of the $MAPbI_3$ perovskite film [62]. Therefore, the increase of the electron quasi-Fermi level of the GUTS-4-$MAPbI_3$ leads to improved energy band alignment with adjacent with SnO_2, which is likely to facilitate the electron extraction along the $MAPbI_3$/SnO_2 interface, and thus higher V_{oc} and *FF* of the resultant device.

The stability of the reference $MAPbI_3$ device and the GUTS-4-$MAPbI_3$ based device were monitored by measuring their performance every three days (Fig. 8). Both devices show similar stability patterns, where the performance increases in the first few days due to the hole-conductivity enhancement of Spiro-OMeTAD in air. After this, the performance slowly decreases, which is correlated to the degradation of

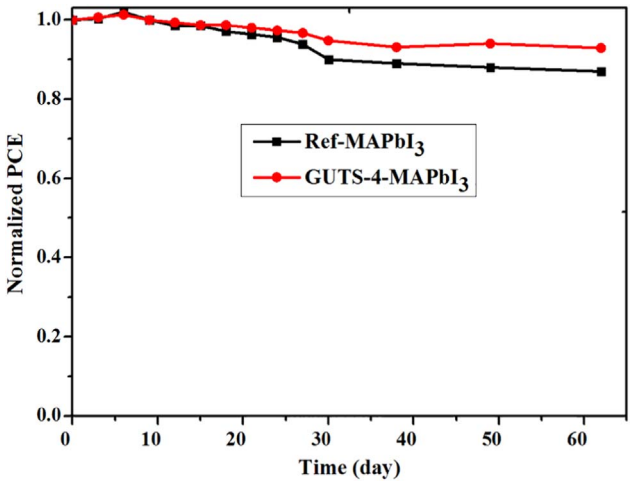

Fig. 8. Moisture stability of the ref-$MAPbI_3$ cell (black curve) and the GUTS-4-$MAPbI_3$ cell (red curve). The solar cells were stored in a desiccator with a relative humidity of ~ 33% in dark. (For interpretation of the references to color in this figure legend, the reader is referred to the web version of this article).

$MAPbI_3$ layer [4]. After 60 days storage in dry air (*RH* 33%), the reference cell retained 87% of PCE while the GUTS-4-$MAPbI_3$ cell

preserved 93% of PCE (Fig. 8). The better moisture stability of the GUTS-4-$MAPbI_3$ cell, as compared to the reference cell could be associated with the better perovskite film quality with less defects, which reduces the probability of water penetration and degradation of perovskites [47,51].

4. Conclusions

We have here demonstrated the effect of GUTS-assisted Ostwald ripening post treatment on the morphology and charge recombination of $MAPbI_3$ film and its interfaces. It was discovered that the concentration of GUTS precursor plays a key role on crystal structure, optical properties, morphology and surface potential of perovskite film. An optimal content of GUTS precursor (GUTS-4, 4 mg/mL) induced micron-sized $MAPbI_3$ film, effectively passivates GBs of $MAPbI_3$ film from recombination and positively shifted the film surface potential as confirmed by KPFM. Further investigation of device recombination kinetics showed that the GUTS-4-$MAPbI_3$ solar cells have higher interfacial charge recombination resistance and lower charge extraction resistance compared to that of the reference $MAPbI_3$ cell, which is in excellent agreement with the results of V_{oc} decay studies. In addition, compared to the pristine $MAPbI_3$, the GUTS-4-$MAPbI_3$ device had lower ideality factor, suggesting less non-radiative recombination. The resultant performance of planar PSCs was improved by 20%, from average PCE of 12.7% for the reference $MAPbI_3$ to 15.2% for GUTS-4-$MAPbI_3$ cells, mainly due to the enhancement of the V_{oc} and *FF*. In addition, devices with GUTS-4-$MAPbI_3$ absorber showed less-pronounced hysteresis in the *J-V* curve and were more inert to moisture than untreated films. This work provides new insight into the mechanism that governs the morphology and optoelectronic properties of $MAPbI_3$ film for high energy conversion efficiency.

Acknowledgements

This work was supported by Australian Research Council Future Fellowship (FT120100674) and Queensland-Chinese Academy of Science (Q-CAS) collaborative research fund. N.D.P thanks Queensland University of Technology (QUT) postgraduate scholarship and CSIRO top-up scholarship. The data of XRD, SEM reported in this paper were obtained at the Central Analytical Research facility (CARF), QUT. Access to CARF was supported by the generous funding from Science and Engineering faculty, QUT. In addition, we acknowledge the measurement of KPFM by the Queensland node of the Australian national Fabrication Facility (ANFF), a company established under the National Collaborative Research Infrastructure Strategy. We thank financial support by MINECO of Spain under project (MAT2013-47192-C3-1-R), and Generalitat Valenciana (ACOMP/2015/105). A.G. would like to thank the Spanish Ministerio de Economía y Competitividad for a Ramón y Cajal Fellowship (RYC-2014-16809).

Appendix A. Supplementary material

Supplementary data associated with this article can be found in the online version at http://dx.doi.org/10.1016/j.nanoen.2017.10.006.

References

[1] M. Gratzel, The light and shade of perovskite solar cells, Nat. Mater. 13 (2014) 838–842.
[2] A. Kojima, K. Teshima, Y. Shirai, T. Miyasaka, Organometal halide perovskites as visible-light sensitizers for photovoltaic cells, J. Am. Chem. Soc. 131 (2009) 6050–6051.
[3] W.S. Yang, B.-W. Park, E.H. Jung, N.J. Jeon, Y.C. Kim, D.U. Lee, S.S. Shin, J. Seo, E.K. Kim, J.H. Noh, S.I. Seok, Iodide management in formamidinium-lead-halide–based perovskite layers for efficient solar cells, Science 356 (2017) 1376–1379.
[4] M.M. Lee, J. Teuscher, T. Miyasaka, T.N. Murakami, H.J. Snaith, Efficient hybrid solar cells based on meso-superstructured organometal halide perovskites, Science 338 (2012) 643–647.
[5] I. Chung, B. Lee, J. He, R.P.H. Chang, M.G. Kanatzidis, All-solid-state dye-sensitized solar cells with high efficiency, Nature 485 (2012) 486–489.
[6] M. Liu, M.B. Johnston, H.J. Snaith, Efficient planar heterojunction perovskite solar cells by vapour deposition, Nature 501 (2013) 395–398.
[7] M. Saliba, T. Matsui, J.-Y. Seo, K. Domanski, J.-P. Correa-Baena, M.K. Nazeeruddin, S.M. Zakeeruddin, W. Tress, A. Abate, A. Hagfeldt, M. Gratzel, Cesium-containing triple cation perovskite solar cells: improved stability, reproducibility and high efficiency, Energy Environ. Sci. 9 (2016) 1989–1997.
[8] N.J. Jeon, J.H. Noh, Y.C. Kim, W.S. Yang, S. Ryu, S.I. Seok, Solvent engineering for high-performance inorganic–organic hybrid perovskite solar cells, Nat. Mater. 13 (2014) 897–903.
[9] N. Ahn, D.-Y. Son, I.-H. Jang, S.M. Kang, M. Choi, N.-G. Park, Highly reproducible perovskite solar cells with average efficiency of 18.3% and best efficiency of 19.7% fabricated via lewis base adduct of lead(II) iodide, J. Am. Chem. Soc. 137 (2015) 8696–8699.
[10] N.D. Pham, V.T. Tiong, P. Chen, L. Wang, G. Wilson, J.M. Bell, H. Wang, Enhanced perovskite electronic properties via a modified lead(II) chloride lewis acid-base adduct and their effect in high-efficiency perovskite solar cells, J. Mater. Chem. A (2017).
[11] C. Bi, Q. Wang, Y. Shao, Y. Yuan, Z. Xiao, J. Huang, Non-wetting surface-driven high-aspect-ratio crystalline grain growth for efficient hybrid perovskite solar cells, Nat. Commun. 6 (2015) 7747.
[12] Y. Shao, Y. Fang, T. Li, Q. Wang, Q. Dong, Y. Deng, Y. Yuan, H. Wei, M. Wang, A. Gruverman, J. Shield, J. Huang, Grain boundary dominated ion migration in polycrystalline organic-inorganic halide perovskite films, Energy Environ. Sci. 9 (2016) 1752–1759.
[13] J.S. Yun, J. Seidel, J. Kim, A.M. Soufiani, S. Huang, J. Lau, N.J. Jeon, S.I. Seok, M.A. Green, A. Ho-Baillie, Critical role of grain boundaries for ion migration in formamidinium and methylammonium lead halide perovskite solar cells, Adv. Energy Mater. 6 (2016) 1600330.
[14] W.-J. Yin, T. Shi, Y. Yan, Unusual defect physics in CH3NH3PbI3 perovskite solar cell absorber, Appl. Phys. Lett. 104 (2014) 063903.
[15] H.-S. Duan, H. Zhou, Q. Chen, P. Sun, S. Luo, T.-B. Song, B. Bob, Y. Yang, The identification and characterization of defect states in hybrid organic-inorganic perovskite photovoltaics, Phys. Chem. Chem. Phys. 17 (2015) 112–116.
[16] P. Xu, S. Chen, H.-J. Xiang, X.-G. Gong, S.-H. Wei, Influence of defects and synthesis conditions on the photovoltaic performance of perovskite semiconductor CsSnI3, Chem. Mater. 26 (2014) 6068–6072.
[17] W.E.I. Sha, X. Ren, L. Chen, W.C.H. Choy, The efficiency limit of CH3NH3PbI3 perovskite solar cells, Appl. Phys. Lett. 106 (2015) 221104.
[18] S. van Reenen, M. Kemerink, H.J. Snaith, Modeling anomalous hysteresis in perovskite solar cells, J. Phys. Chem. Lett. 6 (2015) 3808–3814.
[19] W. Nie, H. Tsai, R. Asadpour, J.-C. Blancon, A.J. Neukirch, G. Gupta, J.J. Crochet, M. Chhowalla, S. Tretiak, M.A. Alam, H.-L. Wang, A.D. Mohite, High-efficiency solution-processed perovskite solar cells with millimeter-scale grains, Science 347 (2015) 522–525.
[20] M. Yang, Y. Zhou, Y. Zeng, C.-S. Jiang, N.P. Padture, K. Zhu, Square-centimeter solution-processed planar CH3NH3PbI3 perovskite solar cells with efficiency exceeding 15%, Adv. Mater. 27 (2015) 6363–6370.
[21] Y.C. Kim, N.J. Jeon, J.H. Noh, W.S. Yang, J. Seo, J.S. Yun, A. Ho-Baillie, S. Huang, M.A. Green, J. Seidel, T.K. Ahn, S.I. Seok, Beneficial effects of PbI2 incorporated in organo-lead halide perovskite solar cells, Adv. Energy Mater. 6 (2016) 1502104.
[22] C. Roldan-Carmona, P. Gratia, I. Zimmermann, G. Grancini, P. Gao, M. Graetzel, M.K. Nazeeruddin, High efficiency methylammonium lead triiodide perovskite solar cells: the relevance of non-stoichiometric precursors, Energy Environ. Sci. 8 (2015) 3550–3556.
[23] H. Yu, F. Wang, F. Xie, W. Li, J. Chen, N. Zhao, The role of chlorine in the formation process of “CH3NH3PbI3-xClx” perovskite, Adv. Funct. Mater. 24 (2014) 7102–7108.
[24] Y. Tidhar, E. Edri, H. Weissman, D. Zohar, G. Hodes, D. Cahen, B. Rybtchinski, S. Kirmayer, Crystallization of methyl ammonium lead halide perovskites: implications for photovoltaic applications, J. Am. Chem. Soc. 136 (2014) 13249–13256.
[25] C. Wang, D. Zhao, Y. Yu, N. Shrestha, C.R. Grice, W. Liao, A.J. Cimaroli, J. Chen, R.J. Ellingson, X. Zhao, Y. Yan, Compositional and morphological engineering of mixed cation perovskite films for highly efficient planar and flexible solar cells with reduced hysteresis, Nano Energy 35 (2017) 223–232.
[26] M.K. Kim, T. Jeon, H.I. Park, J.M. Lee, S.A. Nam, S.O. Kim, Effective control of crystal grain size in CH3NH3PbI3 perovskite solar cells with a pseudohalide Pb(SCN)2 additive, CrystEngComm 18 (2016) 6090–6095.
[27] Y. Yu, C. Wang, C.R. Grice, N. Shrestha, J. Chen, D. Zhao, W. Liao, A.J. Cimaroli, P.J. Roland, R.J. Ellingson, Y. Yan, Improving the performance of formamidinium and cesium lead triiodide perovskite solar cells using lead thiocyanate additives, ChemSusChem 9 (2016) 3288–3297.
[28] W. Ke, C. Xiao, C. Wang, B. Saparov, H.-S. Duan, D. Zhao, Z. Xiao, P. Schulz, S.P. Harvey, W. Liao, W. Meng, Y. Yu, A.J. Cimaroli, C.-S. Jiang, K. Zhu, M. Al-Jassim, G. Fang, D.B. Mitzi, Y. Yan, Employing Lead thiocyanate additive to reduce the hysteresis and boost the fill factor of planar perovskite solar cells, Adv. Mater. 28 (2016) 5214–5221.
[29] Y.-H. Chiang, M.-H. Li, H.-M. Cheng, P.-S. Shen, P. Chen, Mixed cation thiocyanate-based pseudohalide perovskite solar cells with high efficiency and stability, ACS Appl. Mater. Interfaces 9 (2017) 2403–2409.
[30] W. Zhu, C. Bao, Y. Wang, F. Li, X. Zhou, J. Yang, B. Lv, X. Wang, T. Yu, Z. Zou, Coarsening of one-step deposited organolead triiodide perovskite films via Ostwald ripening for high efficiency planar-heterojunction solar cells, Dalton Trans. 45 (2016) 7856–7865.

[31] Z. Xiao, Q. Dong, C. Bi, Y. Shao, Y. Yuan, J. Huang, Solvent annealing of perovskite-induced crystal growth for photovoltaic-device efficiency enhancement, Adv. Mater. 26 (2014) 6503–6509.
[32] M. Yang, T. Zhang, P. Schulz, Z. Li, G. Li, D.H. Kim, N. Guo, J.J. Berry, K. Zhu, Y. Zhao, Facile fabrication of large-grain CH3NH3PbI3−xBrx films for high-efficiency solar cells via CH3NH3Br-selective Ostwald ripening, Nat. Commun. 7 (2016) 12305.
[33] Z. Zhou, Z. Wang, Y. Zhou, S. Pang, D. Wang, H. Xu, Z. Liu, N.P. Padture, G. Cui, Methylamine-gas-induced defect-healing behavior of CH3NH3PbI3 thin films for perovskite solar cells, Angew. Chem. Int. Ed. 54 (2015) 9705–9709.
[34] Y. Jiang, E.J. Juarez-Perez, Q. Ge, S. Wang, M.R. Leyden, L.K. Ono, S.R. Raga, J. Hu, Y. Qi, Post-annealing of MAPbI3 perovskite films with methylamine for efficient perovskite solar cells, Mater. Horiz. 3 (2016) 548–555.
[35] Y. Shao, Z. Xiao, C. Bi, Y. Yuan, J. Huang, Origin and elimination of photocurrent hysteresis by fullerene passivation in CH3NH3PbI3 planar heterojunction solar cells, Nat. Commun. 5 (2014) 5784.
[36] J. Xu, A. Buin, A.H. Ip, W. Li, O. Voznyy, R. Comin, M. Yuan, S. Jeon, Z. Ning, J.J. McDowell, P. Kanjanaboos, J.-P. Sun, X. Lan, L.N. Quan, D.H. Kim, I.G. Hill, P. Maksymovych, E.H. Sargent, Perovskite–Fullerene Hybrid Materials Suppress Hysteresis in Planar Diodes, 6, 2015, p. 7081.
[37] P.-W. Liang, C.-C. Chueh, S.T. Williams, A.K.Y. Jen, Roles of fullerene-based interlayers in enhancing the performance of organometal perovskite thin-film solar cells, Adv. Energy Mater. 5 (2015) 1402321.
[38] D. Bi, W. Tress, M.I. Dar, P. Gao, J. Luo, C. Renevier, K. Schenk, A. Abate, F. Giordano, J.-P. Correa Baena, J.-D. Decoppet, S.M. Zakeeruddin, M.K. Nazeeruddin, M. Grätzel, A. Hagfeldt, Efficient luminescent solar cells based on tailored mixed-cation perovskites, Sci. Adv. 2 (2016).
[39] H. Xu, Y. Wu, J. Cui, C. Ni, F. Xu, J. Cai, F. Hong, Z. Fang, W. Wang, J. Zhu, L. Wang, R. Xu, F. Xu, Formation and evolution of the unexpected PbI2 phase at the interface during the growth of evaporated perovskite films, Phys. Chem. Chem. Phys. 18 (2016) 18607–18613.
[40] N.D. Marco, H. Zhou, Q. Chen, P. Sun, Z. Liu, L. Meng, E.-P. Yao, Y. Liu, A. Schiffer, Y. Yang, Guanidinium: a route to enhanced carrier lifetime and open-circuit voltage in hybrid perovskite solar cells, Nano Lett. 16 (2016) 1009–1016.
[41] W. Ke, G. Fang, Q. Liu, L. Xiong, P. Qin, H. Tao, J. Wang, H. Lei, B. Li, J. Wan, G. Yang, Y. Yan, Low-temperature solution-processed tin oxide as an alternative electron transporting layer for efficient perovskite solar cells, J. Am. Chem. Soc. 137 (2015) 6730–6733.
[42] H.A. Harms, N. Tetreault, N. Pellet, M. Bensimon, M. Gratzel, Mesoscopic photosystems for solar light harvesting and conversion: facile and reversible transformation of metal-halide perovskites, Faraday Discuss. 176 (2014) 251–269.
[43] S. Yang, Y. Chen, Y.C. Zheng, X. Chen, Y. Hou, H.G. Yang, Formation of high-quality perovskite thin film for planar heterojunction solar cells, RSC Adv. 5 (2015) 69502–69508.
[44] G. Madras, B.J. McCoy, Denucleation rates during Ostwald ripening: distribution kinetics of unstable clusters, J. Chem. Phys. 117 (2002) 6607–6613.
[45] J.A. Marqusee, J. Ross, Kinetics of phase transitions: theory of Ostwald ripening, J. Chem. Phys. 79 (1983) 373–378.
[46] Q. Jiang, D. Rebollar, J. Gong, E.L. Piacentino, C. Zheng, T. Xu, Pseudohalide-induced moisture tolerance in perovskite CH3NH3Pb(SCN)2I thin films, Angew. Chem. Int. Ed. 54 (2015) 7617–7620.
[47] Z. Liu, J. Hu, H. Jiao, L. Li, G. Zheng, Y. Chen, Y. Huang, Q. Zhang, C. Shen, Q. Chen, H. Zhou, Chemical reduction of intrinsic defects in thicker heterojunction planar perovskite solar cells, Adv. Mater. (2017) 1606774.
[48] N.K. Noel, S.N. Habisreutinger, B. Wenger, M.T. Klug, M.T. Horantner, M.B. Johnston, R.J. Nicholas, D.T. Moore, H.J. Snaith, A low viscosity, low boiling point, clean solvent system for the rapid crystallisation of highly specular perovskite films, Energy Environ. Sci. 10 (2017) 145–152.
[49] A. Guerrero, J. You, C. Aranda, Y.S. Kang, G. Garcia-Belmonte, H. Zhou, J. Bisquert, Y. Yang, Interfacial degradation of planar lead halide perovskite solar cells, ACS Nano 10 (2016) 218–224.
[50] Y. Zhao, K. Zhu, Optical bleaching of perovskite (CH3NH3)PbI3 through room-temperature phase transformation induced by ammonia, Chem. Commun. 50 (2014) 1605–1607.
[51] C.-H. Chiang, M.K. Nazeeruddin, M. Gratzel, C.-G. Wu, The synergistic effect of H2O and DMF towards stable and 20% efficiency inverted perovskite solar cells, Energy Environ. Sci. 10 (2017) 808–817.
[52] Q. Lin, A. Armin, R.C.R. Nagiri, P.L. Burn, P. Meredith, Electro-optics of perovskite solar cells, Nat. Photon 9 (2015) 106–112.
[53] I. Zarazua, G. Han, P.P. Boix, S. Mhaisalkar, F. Fabregat-Santiago, I. Mora-Seró, J. Bisquert, G. Garcia-Belmonte, Surface recombination and collection efficiency in perovskite solar cells from impedance analysis, J. Phys. Chem. Lett. 7 (2016) 5105–5113.
[54] A. Guerrero, G. Garcia-Belmonte, I. Mora-Sero, J. Bisquert, Y.S. Kang, T.J. Jacobsson, J.-P. Correa-Baena, A. Hagfeldt, Properties of contact and bulk impedances in hybrid lead halide perovskite solar cells including inductive loop elements, J. Phys. Chem. C 120 (2016) 8023–8032.
[55] I. Zarazua, J. Bisquert, G. Garcia-Belmonte, Light-induced space-charge accumulation zone as photovoltaic mechanism in perovskite solar cells, J. Phys. Chem. Lett. 7 (2016) 525–528.
[56] J.-P. Correa-Baena, S.-H. Turren-Cruz, W. Tress, A. Hagfeldt, C. Aranda, L. Shooshtari, J. Bisquert, A. Guerrero, Changes from bulk to surface recombination mechanisms between pristine and cycled perovskite solar cells, ACS Energy Lett. 2 (2017) 681–688.
[57] W. Tress, K. Leo, M. Riede, Dominating recombination mechanisms in organic solar cells based on ZnPc and C60, Appl. Phys. Lett. 102 (2013) 163901.
[58] V.V. Brus, F. Lang, J. Bundesmann, S. Seidel, A. Denker, B. Rech, G. Landi, H.C. Neitzert, J. Rappich, N.H. Nickel, Defect dynamics in proton irradiated CH3NH3PbI3 perovskite solar cells, Adv. Electron. Mater. 3 (2017) 1600438.
[59] A. Zaban, M. Greenshtein, J. Bisquert, Determination of the electron lifetime in nanocrystalline dye solar cells by open-circuit voltage decay measurements, ChemPhysChem 4 (2003) 859–864.
[60] R. Ahmed, L. Zhao, A.J. Mozer, G. Will, J. Bell, H. Wang, Enhanced electron lifetime of CdSe/CdS quantum dot (QD) sensitized solar cells using ZnSe core–shell structure with efficient regeneration of quantum dots, J. Phys. Chem. C 119 (2015) 2297–2307.
[61] R. Gottesman, P. Lopez-Varo, L. Gouda, Juan A. Jimenez-Tejada, J. Hu, S. Tirosh, A. Zaban, J. Bisquert, Dynamic phenomena at perovskite/electron-selective contact interface as interpreted from photovoltage decays, Chem 1 (2016) 776–789.
[62] J.P. Correa Baena, L. Steier, W. Tress, M. Saliba, S. Neutzner, T. Matsui, F. Giordano, T.J. Jacobsson, A.R. Srimath Kandada, S.M. Zakeeruddin, A. Petrozza, A. Abate, M.K. Nazeeruddin, M. Gratzel, A. Hagfeldt, Highly efficient planar perovskite solar cells through band alignment engineering, Energy Environ. Sci. 8 (2015) 2928–2934.

Ngoc Duy Pham is currently pursuing a Ph.D. degree at Queensland University of Technology, Australia. His research interest is on development of solution processed organic-inorganic perovskite solar cells.

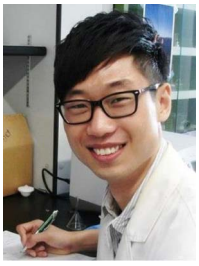

Vincent Tiing Tiong received his M.S. degree from Loughborough University in 2011 and Ph.D. degree in applied science from Queensland University of Technology in 2014. His current research interests include (1) thin film photovoltaic materials and fabrication; (2) nanomaterials and photovoltaic devices engineering.

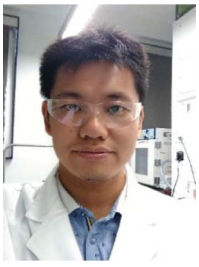

Disheng Yao is a Ph.D. student from School of Chemistry, Physics, mechanical Engineering, Queensland University of Technology. His research focuses mainly on organic-inorganic hybrids perovskite solar cells as the potential renewable energy in the future. He obtained his bachelor degree in Shandong University (2012) and master degree in China's University of Mining and Technology (2016).

Dr Martens completed his Ph.D. in vibration spectroscopy at the Queensland University of Technology (QUT) in 2004. After completing his Ph.D., Dr Martens worked as a chemometrics consultant in the petroleum industry before returning to QUT after winning a Queensland Smart State Fellowship in 2007. Dr Martens has remained at QUT as Senior Lecturer with his research focusses on nanotechnology, interfacial chemistry, chemometrics and vibrational spectroscopy.

Antonio Guerrero is a chemist specialized in semiconductors contracted as a Ramón y Cajal Fellow at the University Jaume I (Spain). Antonio completed a Ph.D. in Organometallic Chemistry industrially funded by Bayer focused on the design of new catalysts for the production of butyl rubber. From 2006 Antonio worked at Cambridge Display Technology where he developed new materials for Organic Light Emitting Diodes applications. In 2010 he joined the group of Prof. Juan Bisquert at INAM. His current research interests include perovskite and organic materials for photovoltaic applications and their use as photoelectrochemical Cells.

Juan Bisquert is a Professor of applied physics at Universitat Jaume I de Castelló, Spain. He is the director of the Institute of Advanced Materials at UJI. He authored 360 peer reviewed papers, and a series of books including *Nanostructured Energy Devices* (1. *Equilibrium Concepts and Kinetics*, 2. *Foundations of Carrier Transport*) and 3. *Physics of Solar Cells: Perovskites, Organics, and Photovoltaics Fundamentals* (CRC Press). He conducts experimental and theoretical research on materials and devices for production and storage of clean energies. His main topics of interest are materials and processes in perovskite solar cells and solar fuel production.

Hongxia Wang is an associate professor and ARC Future Fellow at Queensland University of Technology, Australia. Her main research interest is on development of new routes for low cost solar cells and energy storage devices- work that includes perovskite solar cells, thin film solar cells using earth abundant materials and supercapacitors.